

Parry, L. and Ashcroft, Ian and Wildman, Ricky D. (2016) Understanding the effect of laser scan strategy on residual stress in selective laser melting through thermo-mechanical simulation. *Additive Manufacturing*, 12 (A). pp. 1-15. ISSN 2214-8604

Access from the University of Nottingham repository:

<http://eprints.nottingham.ac.uk/41323/1/ADDMA-D-16-00022.pdf>

Copyright and reuse:

The Nottingham ePrints service makes this work by researchers of the University of Nottingham available open access under the following conditions.

This article is made available under the Creative Commons Attribution Non-commercial No Derivatives licence and may be reused according to the conditions of the licence. For more details see: <http://creativecommons.org/licenses/by-nc-nd/2.5/>

A note on versions:

The version presented here may differ from the published version or from the version of record. If you wish to cite this item you are advised to consult the publisher's version. Please see the repository url above for details on accessing the published version and note that access may require a subscription.

For more information, please contact eprints@nottingham.ac.uk

Manufacturing

Elsevier Editorial System(tm) for Additive

Manuscript Draft

Manuscript Number: ADDMA-D-16-00022

Title: Understanding the Effect of Laser Scan Strategy on Residual Stress in Selective Laser Melting through Thermo-Mechanical Simulation

Article Type: Research paper

Keywords: Selective Laser Melting, SLM, Residual Stress, Simulation, Additive Manufacturing

Corresponding Author: Prof. Ian Anthony Ashcroft,

Corresponding Author's Institution:

First Author: Luke Parry

Order of Authors: Luke Parry; Ian Anthony Ashcroft; Ricky Wildman

Abstract: Selective laser melting (SLM) is an attractive technology, enabling the manufacture of customised, complex metallic designs, with minimal wastage. However, uptake by industry is currently impeded by several technical barriers, such as the control of residual stress, which have a detrimental effect on the manufacturability and integrity of a component. Indirectly, these impose severe design restrictions and reduce the reliability of components, driving up costs. This paper uses a thermo-mechanical model to better understand the effect of laser scan strategy on the generation of residual stress in SLM. A complex interaction between transient thermal history and the build-up of residual stress has been observed in the two laser scan strategies investigated. The temperature gradient mechanism was discovered for the creation of residual stress. The greatest stress component was found to develop parallel to the scan vectors, creating an anisotropic stress distribution in the part. The stress distribution varied between laser scan strategies and the cause has been determined by observing the thermal history during scanning. Using this, proposals are suggested for designing laser scan strategies used in SLM.

Understanding the Effect of Laser Scan Strategy on Residual Stress in Selective Laser Melting through Thermo-Mechanical Simulation

L. Parry, I. A. Ashcroft *, R. D. Wildman

Faculty of Engineering, University of Nottingham, Nottingham, NG7 2RD, UK

* Corresponding author email: ian.ashcroft@nottingham.ac.uk

Keywords: Selective Laser Melting, SLM, Residual Stress, Simulation, Additive Manufacturing

Abstract:

Selective laser melting (SLM) is an attractive technology, enabling the manufacture of customised, complex metallic designs, with minimal wastage. However, uptake by industry is currently impeded by several technical barriers, such as the control of residual stress, which have a detrimental effect on the manufacturability and integrity of a component. Indirectly, these impose severe design restrictions and reduce the reliability of components, driving up costs. This paper uses a thermo-mechanical model to better understand the effect of laser scan strategy on the generation of residual stress in SLM. A complex interaction between transient thermal history and the build-up of residual stress has been observed in the two laser scan strategies investigated. The temperature gradient mechanism was discovered for the creation of residual stress. The greatest stress component was found to develop parallel to the scan vectors, creating an anisotropic stress distribution in the part. The stress distribution varied between laser scan strategies and the cause has been determined by observing the thermal history during scanning. Using this, proposals are suggested for designing laser scan strategies used in SLM.

Nomenclature:

c_p	Specific heat capacity [kJ/kg K]
E	Young's modulus [GPa]
f_{po}	Spot point overlap factor
H	Enthalpy [J]
h_c	Heat transfer coefficient [W/m ² K]
H_p	Plastic Tangent Modulus [GPa]
k	Thermal conductivity [W/m K]
P	Power of laser input [W]
q_s	Surface heat flux [W/m ²]
q_v	Volumetric heat flux [W/m ³]
T	Temperature [°C]
T_A	Temperature (ambient) [°C]
T_L	Temperature (liquidus) [°C]
T_S	Temperature (solidus) [°C]
α	Thermal diffusivity [m ² /s]

α_{th}	Linear thermal expansion coefficient of thermal expansion [1/K]
ϵ	Strain
ϵ_{em}	Emissivity
ν	Poisson's ratio
ρ	Density [g/cm ³]
σ	Stress [MPa]
σ_B	Stefan-Boltzmann constant (5.67x10 ⁻⁸ W/m ² K ⁴)

1 Introduction

Selective Laser Melting (SLM) as an Additive Manufacturing technology has proliferated in interest through enabling designers to realise geometrically complex metallic structures [1], with a rapid design to manufacture cycle compared with conventional manufacturing methods [2]. Owing to its ability to incorporate advanced design techniques, such as topology optimisation [3,4] and lattice structures into components [5], and individual customisation, SLM has gained significant attention from many industrial sectors, in particular aerospace and automotive. Despite its great potential, technical barriers prevent manufacture 'right first time' and impose several manufacturing constraints that reduce design freedoms and design optimization unnecessarily.

The SLM process belongs to the family of powder-bed fusion technologies [6] whereby a powder bed is exposed to a laser beam with a high density flux, causing the powder to fully melt and solidify upon cooling. Laser based manufacturing methods generate large temperature gradients in the vicinity of the applied exposure area owing to the high energy density input. The effect of non-uniform thermal expansions and contractions in the Heat Affected Zone (HAZ) result in the formation of residual stresses in the finished part. Unmanaged, these may have the immediate consequence of causing failure during manufacture, as shown in Figure 1, or other undesirable artefacts of residual stress, including distortion, increased susceptibility to crack formation and reduced fatigue performance [7].



Figure 1 - Failure during manufacturing of a Ti-6Al-4V component caused by the build-up of residual stress.

Parts produced by SLM generally require additional support structures to constrain the part to restrict 'curling' or distortion during manufacture. After manufacture, the relief of residual stress requires further post processing either by heat treatment or hot isostatic pressing (HIP) [8].

A method to mitigate the need for support structures was proposed in [9] by utilising the eutectic point of a zinc alloy (Bi_3Zn) to minimise the melt temperature required thereby reducing the direct energy input. This enabled them to build parts without support structures although they did not report the effects of distortion caused by residual stress. This method is, however, considerably limited in the choice of alloys usable.

The correct choice of laser scan strategy is critical in generating the desired microstructure [10,11] and is also known to affect the build-up of residual stress in components [12]. Previous studies have observed that the largest planar residual stress component is generated parallel to the scan vector and increases with scan vector length [12–14]. Another study investigated the effect of material properties on the creation of residual stress, however, failed to reveal any systematic correlations [15]. Despite this previous work indicating the importance of residual stress generation in SLM, the underlying mechanisms for the generation of residual stress remains little understood. In order to better determine the factors influencing the build-up of residual stress, thermo-mechanical models for simulating SLM are potentially valuable, although this is challenging due to the complexity of the physics involved in the SLM process and the multiple analytical scale lengths.

Previous research in simulating SLM has focused on modelling the thermal transport behaviour in SLM and EBM, with relatively few studies that couple this with the mechanical response. General coupled thermo-mechanical analyses of SLM have been reported by several authors [16–19], but these did not examine in detail the effects of laser scan strategy and are mainly focused on

1 developing modelling techniques. Observations from such simulations have included the reporting of
2 an asymmetric melt-pool and that the largest stress component was generated parallel to the
3 scanning direction, agreeing with previous experimental studies [14]. Another approach that has
4 been proposed is applying an instantaneous, uniform heat flux to the entire cross-sectional surface,
5 rather than simulating the motion of the laser path [20,21]. However, this method is limited by its
6 inability to resolve the effect of laser scan strategy on residual stress. To overcome this limitation, a
7 layer based model using a characteristic strain determined using a macro scale model has been
8 proposed [22].
9

10
11 Computational Fluid Dynamics (CFD) coupled with a FE analysis has been used to account for
12 thermo-fluid effects inside the melt pool but due to their inherent computational cost are limited to
13 mesoscale simulations for small time scales [23–26]. Hodge et al. [18] advanced this area by
14 incorporating a multi-phase stress term using volumetric fractions, and a phase expansion term to
15 account for volumetric shrinkage during phase change between powder and consolidated form.
16
17

18
19 Current models have not identified the geometrical relationship between the choices of laser scan
20 strategy with the generation of residual stress. Also, there is a lack of knowledge relating the
21 temperature field created with the residual stress generated by the choice of laser scan strategy.
22 Currently this information is not available in a way that would enable the prediction of distortion and
23 failure, and consequently, the reliable manufacture of components in SLM.
24
25

26
27 In this paper, a coupled thermo-mechanical finite element model is established to determine the
28 mechanisms that cause the generation residual stress during SLM. The model is then used to
29 determine the implications of the temperature history, created by the choice of laser scan strategy
30 and scan area size, on the development of residual stress during selective laser melting. This work
31 sets the basis for the development of optimal scan strategies to mitigate residual stress effects in
32 SLM built components.
33
34

35 36 37 **2 Model Definition** 38 39

40 **2.1 Simulation Overview**

41 This work uses a coupled thermo-mechanical finite element (FE) analysis for the simulation of the
42 SLM of Ti-6Al-4V with laser parameters chosen specifically for manufacture on a Realizer SLM-50
43 [27]. A commercial FE solution was deemed sufficient to provide a robust solution whilst reducing
44 development time required. MSC Marc [28] was chosen because of its competency in modelling
45 non-linear multi-physics manufacturing processes and the ability to extend models and functionality
46 with user defined Fortran subroutines
47
48
49

50
51 The overall modelling strategy attempts to replicate the SLM process by directly simulating the
52 machine build files to enable a direct comparison with experiments. The workflow is shown in Figure
53 2 where it can be seen that two main inputs are required: an extensive list of material properties and
54 the machine build file.
55
56
57
58
59
60
61
62
63
64
65

1
2
3
4
5
6
7
8
9
10
11
12
13
14
15
16
17
18
19
20
21
22
23
24
25
26
27
28
29
30
31
32
33
34
35
36
37
38
39
40
41
42
43
44
45
46
47
48
49
50
51
52
53
54
55
56
57
58
59
60
61
62
63
64
65

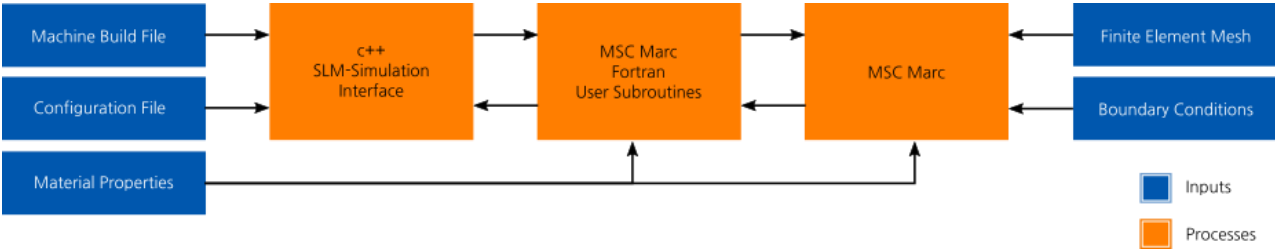


Figure 2 - An overview of inputs required by the simulation and the interdependency of processes

The simulation process interacts between Fortran user subroutines and an external c++ interface to control the simulation behaviour whilst running (Figure 3). The c++ interface has several responsibilities. Firstly, it parses the machine build file and controls the laser position, laser power and state at a given simulation time. Secondly, it manages the adaptive time-stepping procedure ensuring that a consistent time step is used for varying laser scan speeds (Section 2.3). Finally, it provides an interface for managing the state variable of each element. This functionality is integrated separately with a general purpose, multi-physics FE solver to enable future additions of more complex modelling.

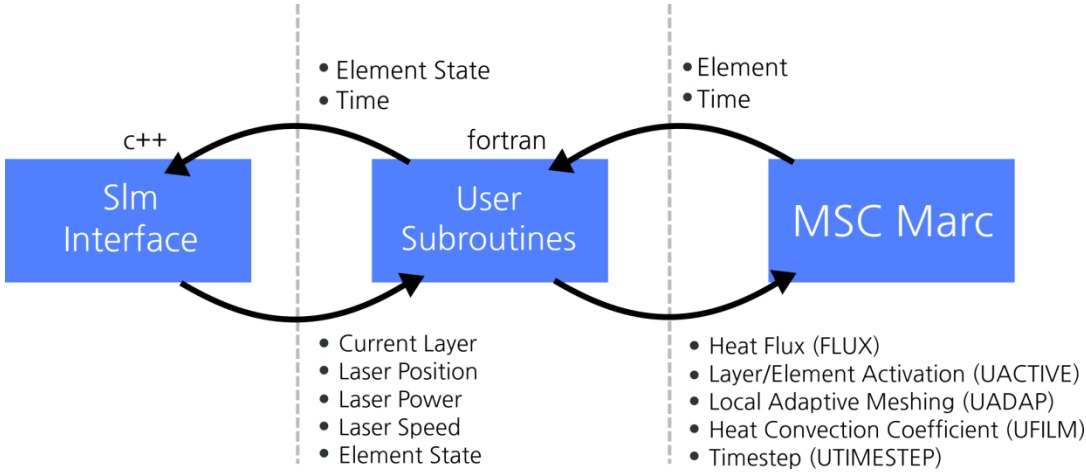


Figure 3 - The interaction between c++ interface, Fortran user subroutines and MSC Marc.

2.2 Thermal Definition

The thermal problem is governed by the enthalpy within a system, defined as

$$H = \int_{T_{ref}}^T \rho c_p dT \tag{1}$$

with the heat transfer defined by the heat equation in a volume, Ω , as given in equation (2).

$$\frac{\partial H}{\partial t} = \nabla(k(T)\nabla T) + q_v + q_s, \text{ in } \Omega. \tag{2}$$

The volumetric heat input term, q_v , is the heat input from the laser source defined in equation (6). The surface heat source term, q_s , is the sum of the convective and radiation terms defined in equation (3), which was applied to the exposed powder bed surface, Γ , having a surface normal \mathbf{n} such that

$$k(T) \frac{\partial T}{\partial \mathbf{n}} = +h_c(T - T_A) + \epsilon_{em} \sigma_B (T^4 - T_A^4) \text{ on } d\Gamma. \quad (3)$$

The values of emissivity ϵ_{em} used in equation (3) in this work were compiled using two sources, as shown in Table 1 and a heat convection coefficient, $h_c = 14.73 \text{ W/m}^2\text{K}$ [29] was used.

Temperature [°C]	Emissivity ϵ_{em}
25	0.121
100	0.155
200	0.178
300	0.205
400	0.228
500	0.331
600	0.561
700	0.591
900	0.600
1500	0.600
1650	0.405
1900	0.402
2100	0.400
2300	0.398
2600	0.395

Table 1 - Temperature dependent emissivity values used for both powder and solid compiled from two sources [30,31].

Three material phases were considered in the simulation: powder, solid and liquid. Both the liquid and solid state represent the 'consolidated' form. A unidirectional transformation occurs during consolidation from powder to liquid and there is a bidirectional transformation between solid and liquid during (re)melt. Each state requires a set of temperature dependent material properties, with the powder state having an assumed packing factor of 0.6 [19].

In order to assign appropriate material properties, a state variable was used to track the state of each element, using a discrete variable ϕ with the three exclusive conditions

$$\phi = \begin{cases} -1 & \text{Powder State} \\ 0 & \text{Liquid State} \\ 1 & \text{Solid State} \end{cases} \quad (4)$$

During the transition to the liquid phase, stresses and any previously accumulated strains were reset by becoming temporarily deactivated during the simulation to emulate annealing and prevent unrealistic accumulation of plastic strains.

Independent measurements of thermal diffusivity were gathered for Ti-6Al-4V powder and solid AM samples. Both samples were tested using a Netzsch LFA 427 laser flash analysis machine under a vacuum atmosphere purged with an argon backflow from room temperature up to 1400 °C. A cylindrical specimen with a diameter of 12.7 mm and 2 mm depth was prepared using the Realizer SLM 50 to measure the diffusivity of the solid specimen. The powder sample was placed inside an 85 μ L sapphire crucible and spray coated with graphite on the top and bottom surfaces to increase absorptivity and emissivity of the sample. Thermal conductivity values were calculated from the measured thermal diffusivity in conjunction with density and specific heat capacity according to

$$k = \alpha c_p \rho. \quad (5)$$

Thermal conductivity values for the liquid state were taken from experiments performed by Bovineau et al. [31]. The thermal conductivity values for all states are presented in Figure 4 and the supporting properties required for its calculation are listed in Table 2 and Table 3.

Temperature [°C]	Specific heat capacity c_p [J/kgK]	Density ρ [g/cm ³]	Thermal Diffusivity α [m ² /s]	Thermal conductivity k [W/m K]
20	520	2.65	0.11	0.145
100	516	2.65	0.09	0.125
200	505	2.64	0.08	0.104
300	492	2.63	0.07	0.092
400	480	2.62	0.07	0.083
500	473	2.61	0.06	0.078
600	472	2.60	0.14	0.167
700	483	2.59	0.17	0.216
800	507	2.58	0.21	0.279
900	548	2.57	0.31	0.430
1000	610	2.56	0.52	0.813
1100	696	2.55	0.53	0.934
1200	808	2.54	0.53	1.09
1300	951	2.53	0.53	1.27

Table 2 -Temperature dependent material properties used for the powder form of Ti-6Al-4V. Specific heat capacity and density taken from [32].

Temperature [°C]	Specific heat capacity c_p [J/kgK]	Density ρ [g/cm ³]	Thermal Diffusivity α [m ² /s]	Thermal conductivity k [W/m K]
20	543	4.42	2.95	7.07
200	566	4.39	3.74	9.28
400	599	4.36	4.51	11.8
600	636	4.33	5.25	14.5
800	675	4.30	5.98	17.4
1000	713	4.27	7.22	22.0
1200	745	4.24	7.91	25.0

1400	770	4.21	8.02	26.0
------	-----	------	------	------

Table 3 - Temperature dependent material properties used for solid Ti-6Al-4V. Specific heat capacity and density taken from [32].

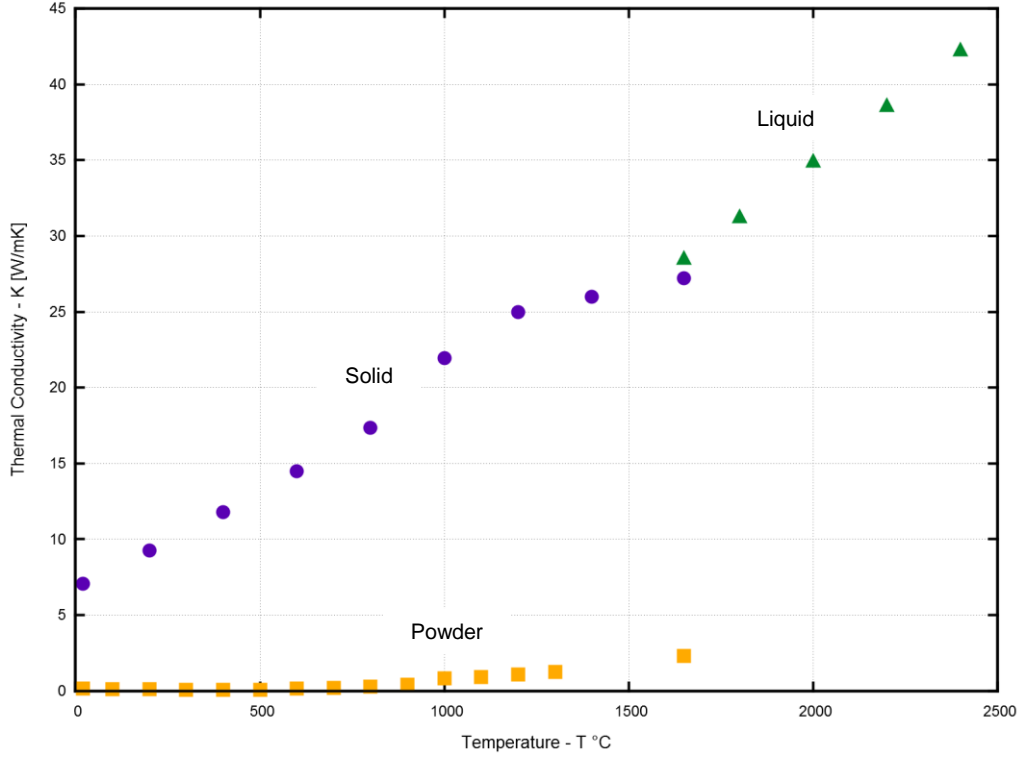


Figure 4 - Compiled thermal conductivity values for the powder, solid and liquid states of Ti-6Al-4V.

2.3 Laser Heat Input

The laser heat input was modelled using the volumetric Gaussian heat source proposed by Goldak [33] with the definition

$$q = \frac{6\eta\sqrt{3}P}{\pi\sqrt{\pi}r_x r_y r_z} e^{-\frac{3x^2}{r_x^2}} e^{-\frac{3y^2}{r_y^2}} e^{-\frac{3z^2}{r_z^2}} \quad (6)$$

with a variable laser power P , laser spot radii r_x , r_y , and r_z , and a lumped efficiency term η to account for the relative absorption of laser energy into the material. Caution is expressed when choosing η because these values vary widely between experimental studies for both powder and solid medium [19]. For powder, this is assumed to be the same as pure titanium powder $\eta = 0.77$ [34] and for the solid substrate is assumed to be $\eta = 0.3$ [35]. Normally, to account for latent heat, the specific heat is modified in a finite interval between the solidus T_S and liquidus T_L temperatures. This was excluded in this work because accounting for latent heat requires a small enough time-step to ensure the temperature change does not overshoot this interval and is relatively insignificant compared with loss of heat through radiation.

The transmission efficiency of the laser source in SLM has not been accurately measured, both in general and specifically for the Realizer SLM 50. It is expected that many factors during the build will affect this, such as the release of a metal condensate into the path of the laser [36] or the lens focal position. Hence, the inclusion of empirical laser absorption efficiency term in this work.

A constant point overlap factor f_{po} was used to control the relative position of the laser point between each simulation time step, as shown in equation (7). This ensures that irrespective of the laser speed, v , and the fixed laser spot size, r_d , the heat flux traverses across the whole scan path without any intermittent gaps.

$$\Delta t = \frac{f_{po} r_d}{v} \quad (7)$$

2.4 Mechanical Definition

The structural analysis assumes a small strain and small deformation formulation using an elasto-plastic constitutive model with the standard relation

$$\{\sigma\} = [D]\{\varepsilon\} \quad (8)$$

with Cauchy stress σ , and D the element stiffness matrix. The total strain tensor, ε , is the superposition of three strains terms

$$\varepsilon = \varepsilon_E + \varepsilon_P + \varepsilon_{th} \quad (9)$$

which are the elastic strain, ε_E , plastic strain, ε_P , and the thermal strain, ε_{th} . The latter defined as

$$\varepsilon_{th}(T) = \int_{T_{Ref}}^T \alpha_{th}(T) dT \quad (10)$$

The linear coefficient of thermal expansion, α_{th} , is listed in Table 4 for Ti-6Al-4V. The Poisson's ratio is assumed to be $\nu = 0.342$ and $\nu = 0.5$ in the elastic and plastic regimes, respectively [37,38].

For modelling time-independent plasticity, a kinematic plasticity model with a von Mises yield criterion was chosen as this captures the cyclic non-linear work hardening (Baushinger) effect [39]. Temperature dependent properties for the yield stress σ_Y and the plastic tangent modulus H_P are listed in Table 4.

Temperature [°C]	Linear CTE $\times 10^{-6}$ [1/K]	Young's modulus E [GPa]	Yield stress σ_Y [MPa]	Plastic tangent modulus H_P [GPa]
24	8.78	125	1000	0.7
94	9.83	110	630	2.2
205	10.0	100	630	2.2
317	10.7	100	525	2.2
428	11.1	80	500	1.9
539	11.2	74	446	1.9
650	11.7	55	300	1.9

761	12.2	27	45	2
872	12.3	20	25	2
1094	12.4	5	5	2
1650*	12.5	0.1	0.1	0.1

Table 4 - Temperature dependent mechanical properties for bulk Ti-6Al-4V [40]. * linearly extrapolated values

The structural pass is performed once the element state has been set and the element connectivity has been calculated to prevent the activation of rigid bodies. Activation of elements during the mechanical pass are only considered for solid elements ($\phi = 1$) and have connectivity with the base plate. If remelting of a previously consolidated elements does occur, the previously accumulated strains for the element are reset to zero and are removed subsequently from the structural analysis pass.

3 Methodology

In order to investigate the importance of the chosen laser scan strategy on the residual stresses in the built component, two scan strategies were chosen: unidirectional and alternating (meander). Both laser paths were generated with a custom Matlab script using compatible laser machine parameters, listed in Table 5, and scan parameters in Table 6.

Laser style configuration	Laser power [W]	Point exposure time [μ s]	Point distance [μ m]	Effective laser speed [mm/s]
Contour (Border)	40.0	40	10	250
Hatching	82.5	40	20	500

Table 5 - Laser style parameters used by a Realizer SLM 50 for Ti-6Al-4V used to generate the machine build files.

Hatch distance [mm]	0.09
Border offset [mm]	0.07
Spot compensation [mm]	0.14
Layer Thickness [mm]	0.04

Table 6 - Parameters used by a Realizer SLM 50 for Ti-6Al-4V to generate the laser geometry in the machine build files.

The hatched region is scanned first followed by the scan of a single outer contour for each case, as illustrated in Figure 5. A direct comparison of the two scanning strategies can be made since the total scanning times are equivalent.

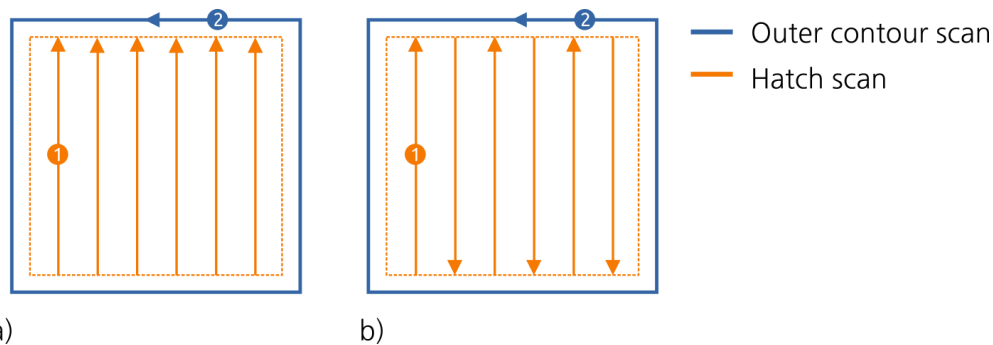


Figure 5 - Laser scan strategies chosen: a) unidirectional and b) alternating

1 The single layer simulations were scanned directly over a solid substrate to enable a comparison
2 with previous work. For each simulation, the domain consisted of a powder bed composed of
3 uniform 0.02 mm 8 noded hexahedral elements and a substrate region with an overall thickness of
4 1.56 mm. The spot overlap factor f_{po} was set to 0.8. The entire domain had an initial temperature
5 set to 200 °C with a cooling time of 5 seconds. Six simulation cases were chosen: two scan strategies
6 with three different cross-sectional widths each (1-3 mm).
7

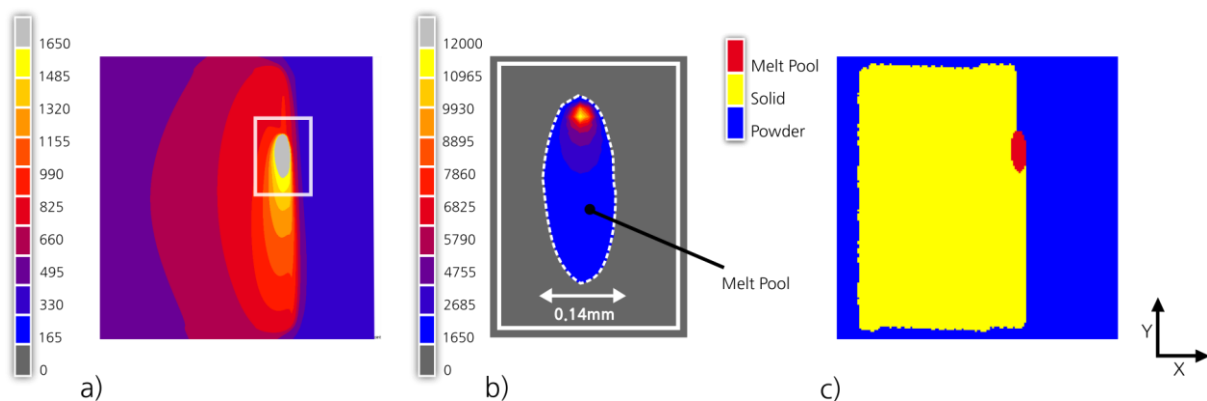
8
9 To validate the thermal simulation, a study was conducted to compare the melted track widths
10 observed experimentally with those found in the simulation results. A 3 mm x 3 mm square region
11 was processed on a Realizer SLM 50 for a single layer using the same parameters as the simulation.
12 An evenly distributed layer was created by manually spreading the powder on the surface of the
13 base plate. Optical measurements were then taken for the melted track widths to be compared with
14 the results obtained from the simulation.
15
16
17

18 4 Results

19 A validation of the thermal analysis with experiment is presented first, in Section 4.1. The effect of
20 scan area size and scan strategy on thermal history is then discussed in Section 4.2, the mechanical
21 response is evaluated in Section 4.3 and, finally, a comparison between the two laser scan strategies
22 is made in Section 4.4.
23
24
25
26
27

28 4.1 Validation of Thermal Analysis with Experiment

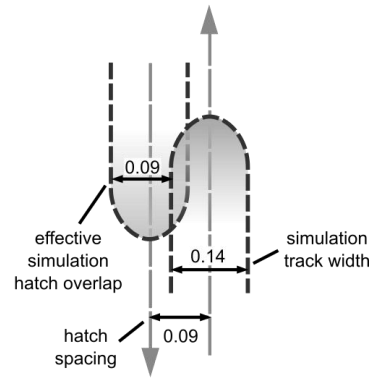
29 The surface temperature for a single scan vector in Figure 6(a) shows an approximate melt-pool
30 width of 0.14 mm. The peak temperature is an isolated singularity inside the melt pool region above
31 the vapourisation temperature of Ti-6Al-4V. A micrograph was taken for the single layer experiment
32 described in Section 3, as shown in Figure 7. It can be seen from comparing Figures 7(a) and 7(b) that
33 the track width in simulation and experiment varies by approximately 14%, taking into account of
34 adjacent track re-melting due to overlap. This provides confidence in the modelling approach and
35 material parameters used in the simulations.
36
37
38
39



54 Figure 6 – Temperature distribution whilst scanning, showing a) the temperature in the hatched region, b) temperature
55 inside the melt pool and c) the element state variable.
56
57
58
59
60
61
62
63
64
65



a)



b)

Figure 7 – a) Single layer laser scan on a base plate using Ti-6Al-4V of adjacent tracks and b) diagram illustrating the calculated overlap of adjacent scan tracks for the simulation.

4.2 Thermal Analysis of Single Layer Sections

Due to the inclusion of multiple material phases, non-symmetric thermal behaviour is seen, as illustrated in Figure 6(a). A resulting asymmetric melt pool is formed during the laser scan in the hatched area due to the position of powder and solid regions on each side of the scan vector, as shown in Figure 6(c). The melt pool becomes asymmetric through preferential heat conduction into the previously scanned consolidated region which has a higher conductivity than the neighbouring powder region.

The transient thermal histories of the simulations are shown in Figure 8 by taking the average temperature for currently solidified elements in the first layer. It can be seen that for all scanned areas, the average temperature decreases with scanning time. The discontinuities in temperature, shown in Figure 8, indicate the change from hatch to contour scan and the end of scanning. Overall, the average element temperature is the highest in the smallest scan area but is held for a short duration, compared with the larger region sustaining a lower temperature over a greater period of time. This is caused by higher thermal losses associated with the higher temperature the smallest region is held at, and the increased storage of thermal energy into the substrate, thereby reducing conductive losses from the consolidated layer. Oscillations in the temperature correspond to the scanning of adjacent tracks and are shown for a single node in 3 mm x 3mm cases in Figure 9. The oscillations resemble a damped 'sawtooth' wave with the peaks corresponding to the position of the laser at the end of each scan vector. The temperature oscillations are damped and tend towards a steady state of 400°C, as a result of the energy balance of the heat input and losses in the system, as defined in equation (2).

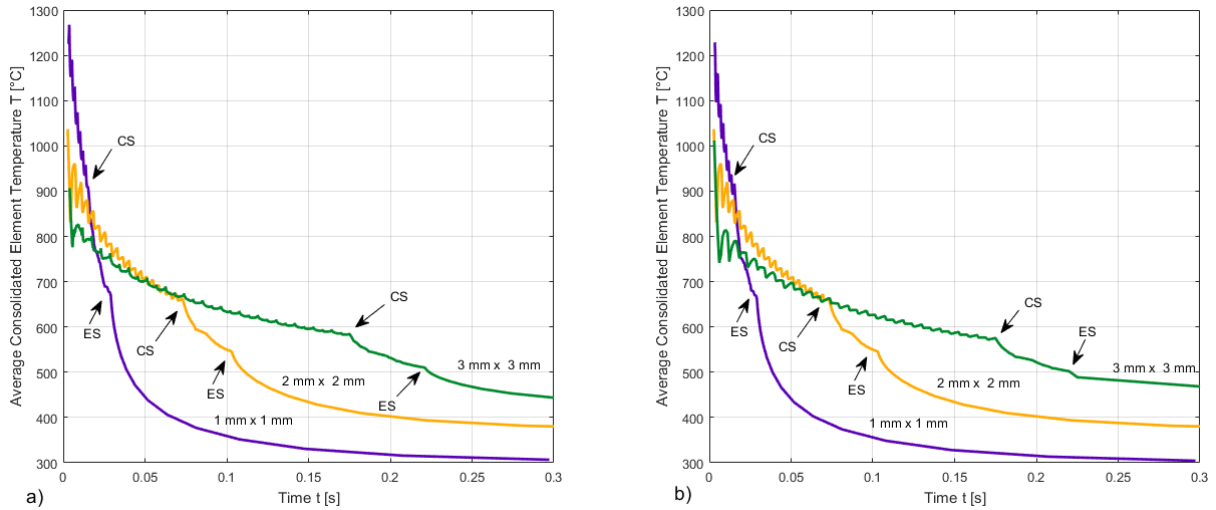


Figure 8 – Average solidified element temperature over time for different scan area sizes cases (CS – Start of the Contour Scan and ES – End of Scanning) for a) alternating and b) unidirectional scan strategy.

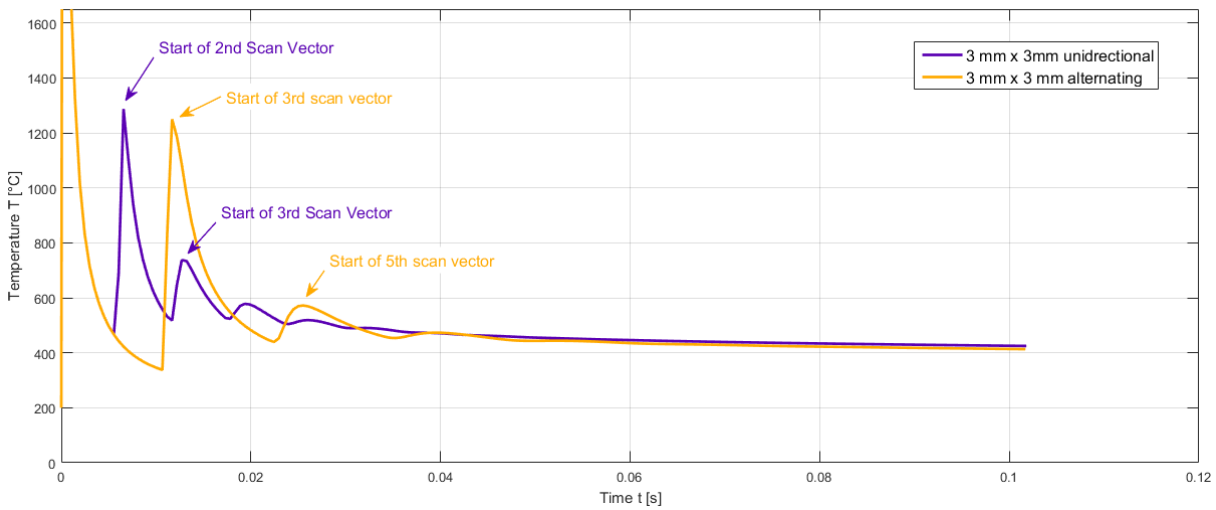


Figure 9 - Temperature profile for a single node taken at top left corner of the hatch region for the unidirectional and alternating scan strategies.

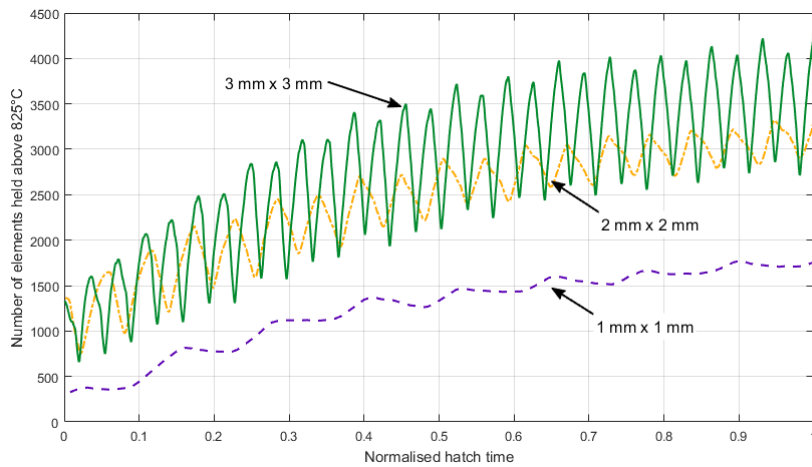


Figure 10 – Total number of elements held above 825 °C the three different scan cases when using the alternating strategy.

In Figure 10, the total area held above 825°C, the point at which Ti-6Al-4V begins to acquire superplastic behaviour [41], increases with time. This indicates the accumulation of heat into the part since the power is kept constant throughout scanning the hatched region.

The probability density distribution $P(T, t)$ in Figure 11 shows the current temperature state throughout the scanning history of the hatched regions. A skewed distribution is present, with the presence of oscillations (ridges) throughout the scanning history in all cases. When scanning the smallest region, as shown in Figure 11(a,d), a large proportion of elements are held above 825°C. Towards the end of scanning, the distributions in the larger regions become narrower, with the peak centred at approximately 500°C. During the early phase of scanning using the alternate strategy, as shown in Figure 11(a,b,c), the troughs in the temperature are lower compared to the unidirectional strategy.

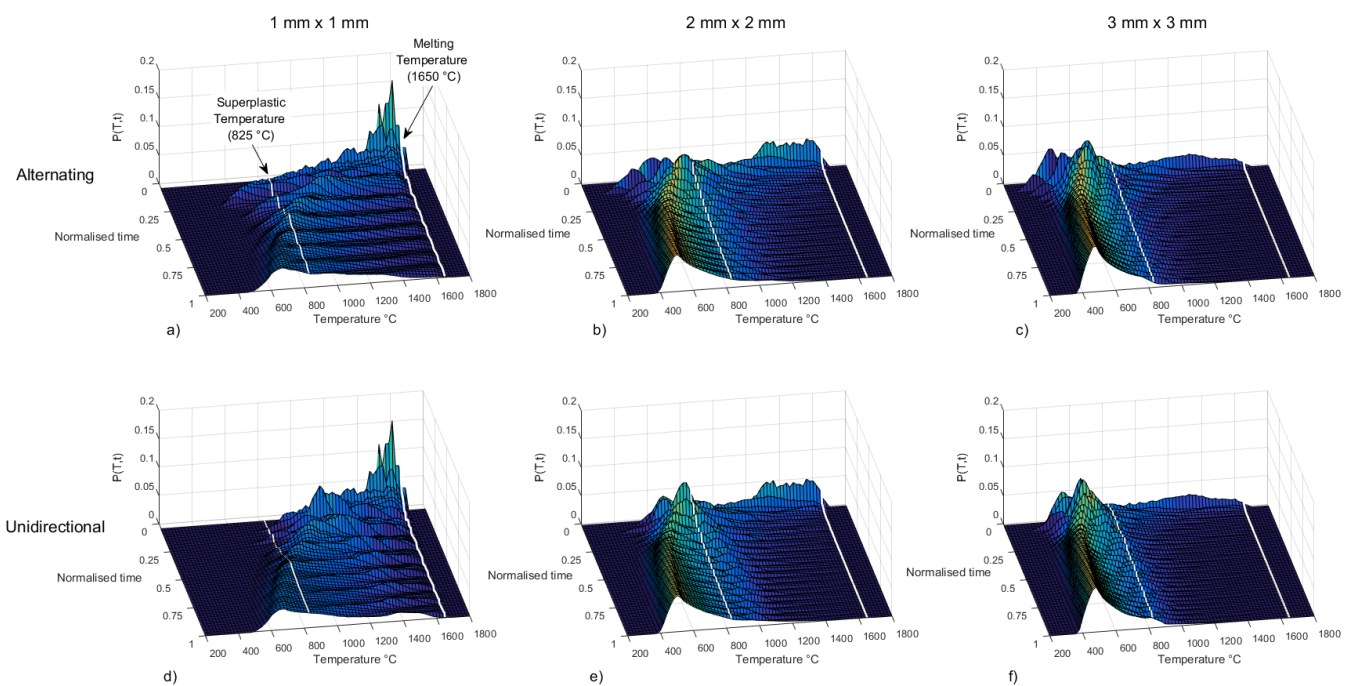


Figure 11 - Transient probability density distribution $P(T,t)$ for consolidated elements normalised to the scanning time of the hatched region. Distributions are shown for the alternating strategy with sizes a) 1 mm x 1 mm, b) 2 mm x 2 mm and c) 3 mm x 3 mm, and unidirectional strategy with sizes d) 1 mm x 1 mm, e) 2 mm x 2 mm and f) 3 mm x 3 mm.

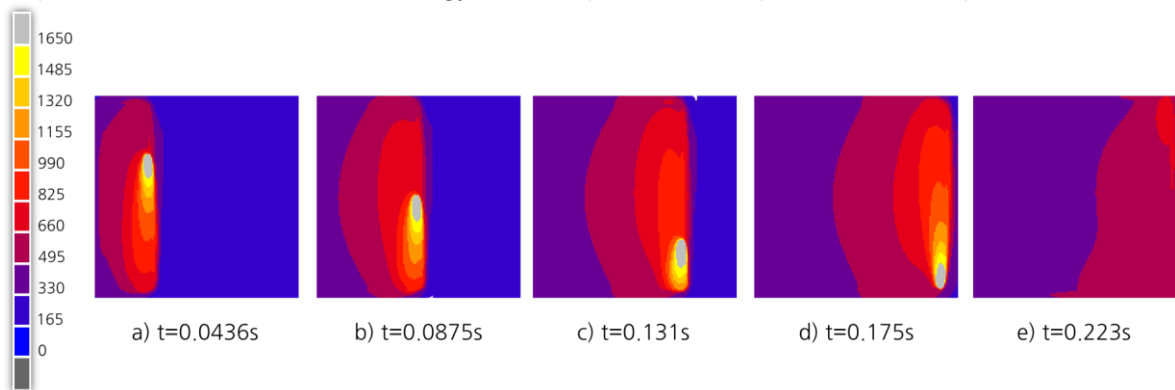


Figure 12 - Profile views of temperature for 3 mm x 3 mm test case using the alternating scan strategy. The time intervals was taken for a) ¼ hatch scan time, b) ½ hatch scan time, c) ¾ hatch scan time, d) end of scanning hatch, and e) the

end of contour scan.

The temperature history for the 3 mm x 3 mm test case with the alternating scan strategy, as illustrated in Figure 12, shows a localised heat tail in the direction of the scan vector, situated near recently scanned tracks. Over time, heat becomes uniformly dissipated into previously consolidated regions.

4.3 Stress Analysis of Single Layer Regions

The state of a single scan vector track at an instance is shown in Figure 13. It can be seen that longitudinal stress, σ_{yy} , as shown in Figure 13(d), is generated as consolidated material behind the melt pool cools and contracts. The transverse stress, σ_{xx} , shown in Figure 13(d) is lower due to the lack of solid material inhibiting thermal expansion and a lower temperature gradient perpendicular than parallel to the scan vector, respectively shown in Figure 13(b) and Figure 13(c)

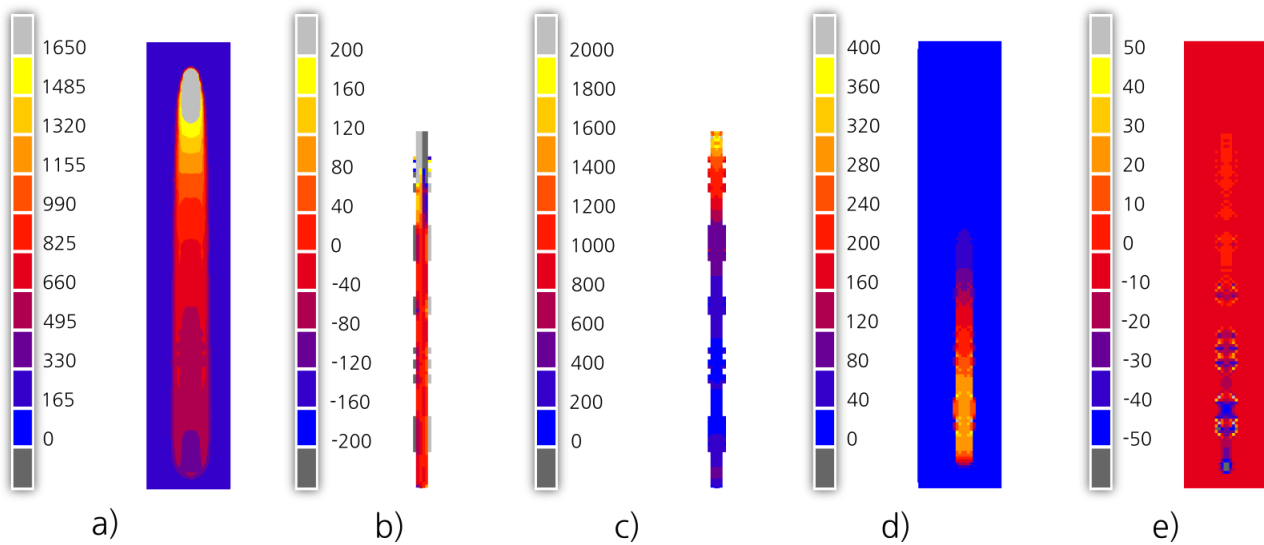


Figure 13 - Profile views during the first scan vector of a) temperature, b) temperature gradient in solid elements in X direction c) temperature gradient in solid elements in Y direction, d) σ_{yy} stress component, and e) σ_{xx} stress component.

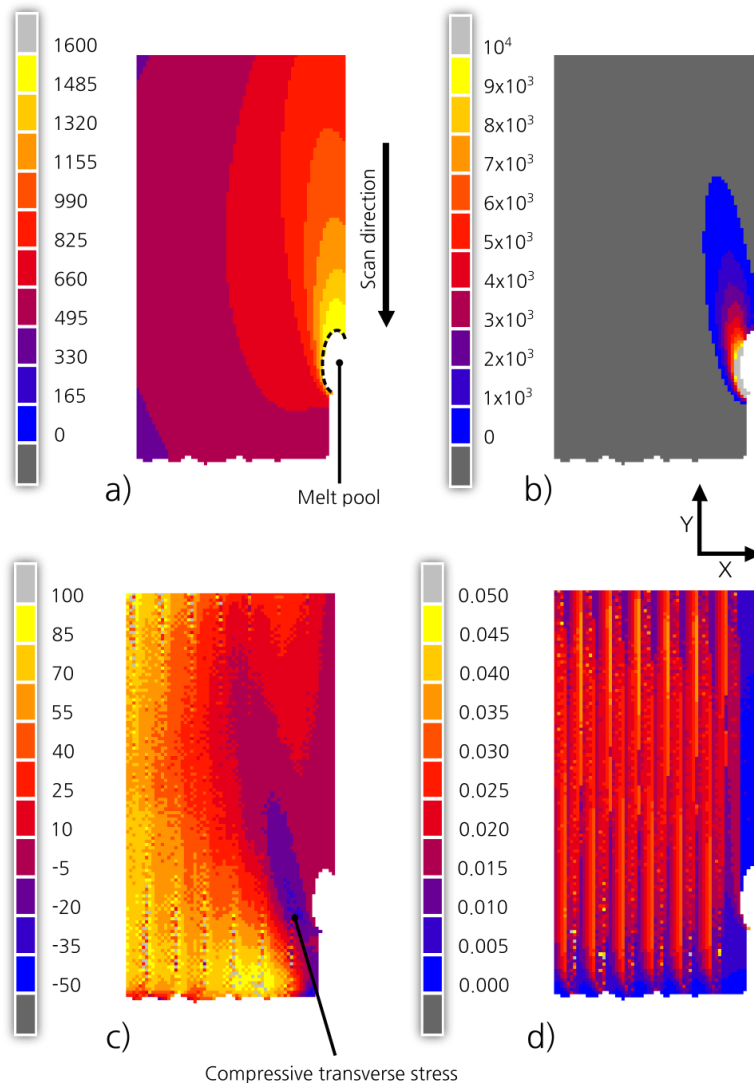
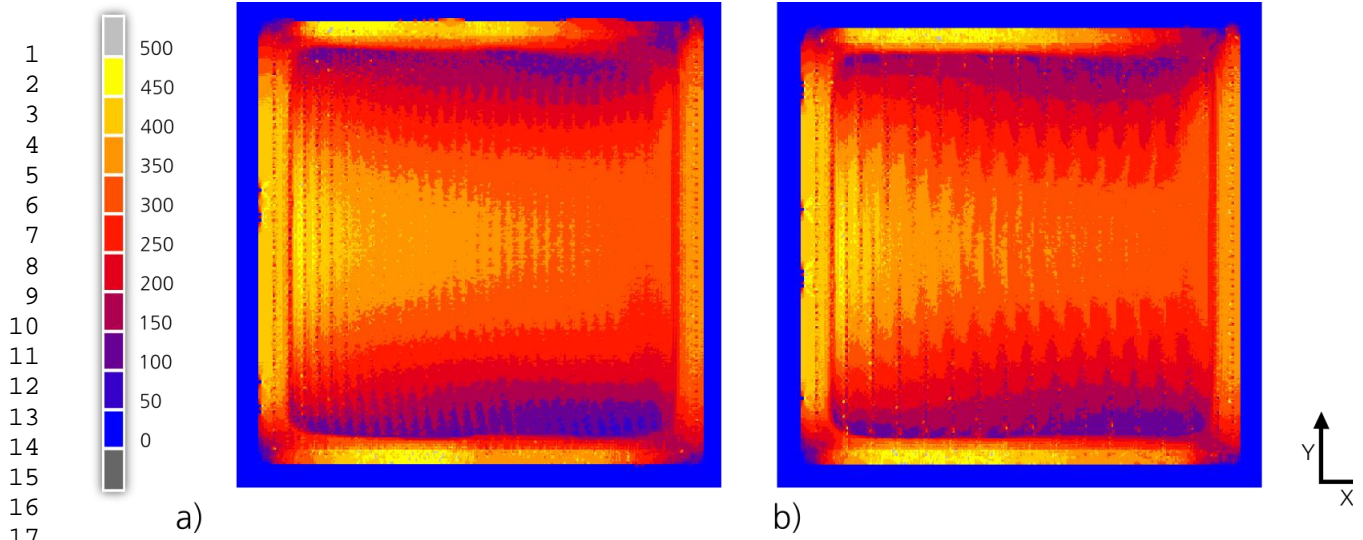


Figure 14 - Profile views of a) temperature b) temperature gradient, c) σ_{xx} [MPa] and d) total equivalent plastic strain whilst scanning the 3 mm x 3 mm unidirectional test case at $t = 0.092s$. Dashed line indicates position of the melt pool region.

Upon the accumulation of several tracks, there is a progressive build-up of transverse stress, as shown in Figure 14(c), due to material inhibiting thermal expansion in the previously scanned track. The thermal expansion in the region surrounding the melt pool creates a compressive stress in the neighbouring region. Due to the high temperature in the HAZ, yielding occurs, which creates regions of plastic strain between each adjacent scan track in the hatch region, as shown in Figure 14(d).

A non-uniform, anisotropic stress distribution in the component is generated, as shown in Figure 15 and Figure 16. The stress distributions in the XY plane are mostly dominated by the σ_{yy} component which decreased in magnitude from the start to the end of the hatched region, as shown in Figure 16(a). The largest σ_{yy} stresses were situated centrally along the hatch region and decrease towards the end of the scan vectors in the hatched region. A 'ripple' effect was observed in both the transverse and longitudinal stress components, when using the alternating scan strategy (Figure 16(a)).



21
22
23
24
25
26
27
28
29
30
31
32
33
34
35
36
37
38
39

Figure 15 - Profiles views of von Mises stress distribution for 3 mm x 3 mm test case when using a) unidirectional, and b) alternating scan strategies.

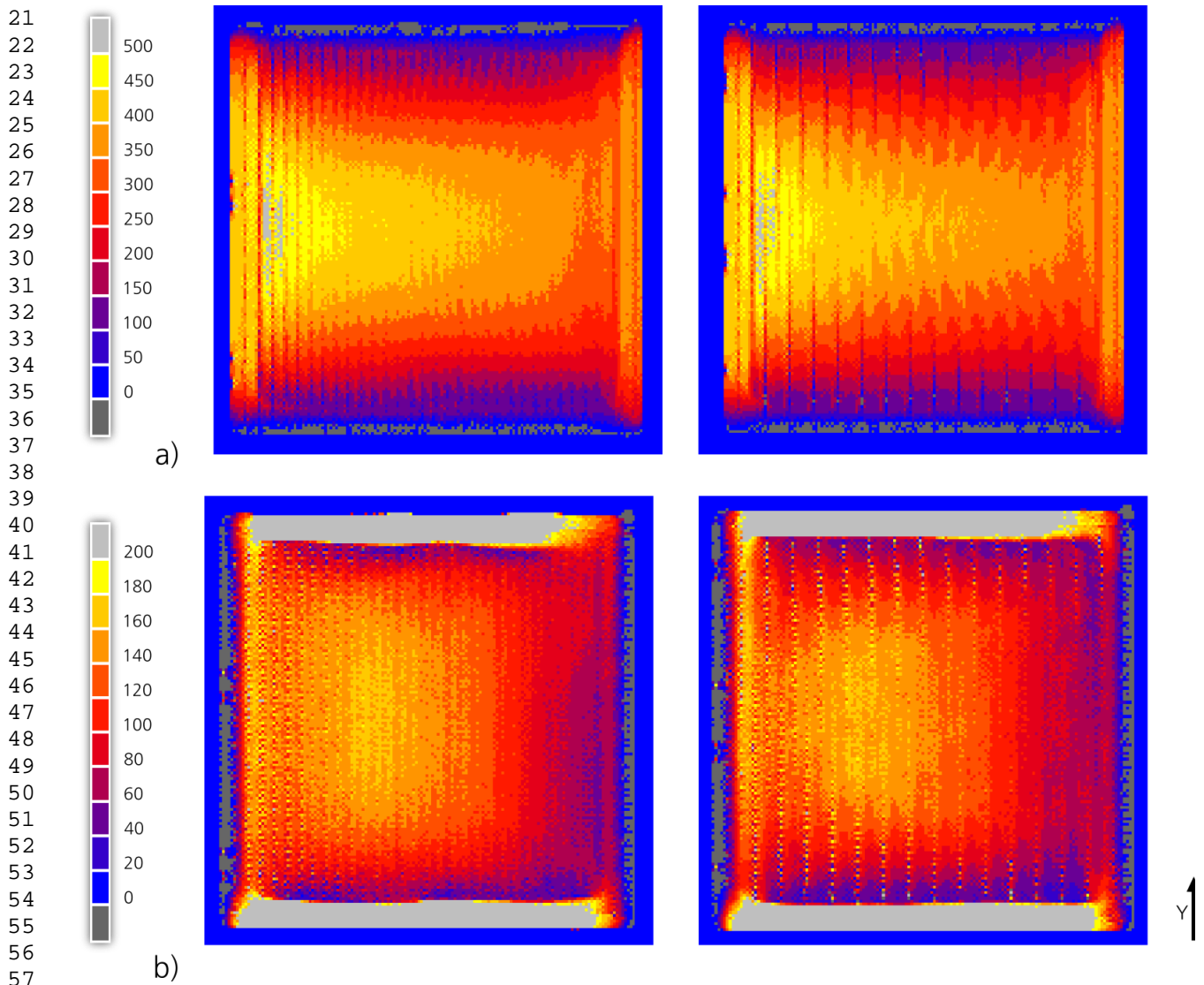


Figure 16 - Profile view of surface normal stresses a) σ_{yy} and b) σ_{xx} when using unidirectional (left) and alternating (right) scan strategies

To identify the cause for the longitudinal stress varying in the X direction for both scan strategies, a series of comparisons were made near the beginning and the end of scanning the hatch region, as shown in Figure 17. Towards the end of scanning the hatched zone, the surrounding region was held at a higher temperature, as shown in Figure 17(a) and exhibited a smaller temperature gradient behind the melt pool region, illustrated in Figure 17(b). During the initial development of the longitudinal stress behind the melt pool, as shown in Figure 17(c), the magnitude of these stresses were found to be lower towards the end of scanning for the hatched region.

1
2
3
4
5
6
7
8
9
10
11
12
13
14
15
16
17
18
19
20
21
22
23
24
25
26
27
28
29
30
31
32
33
34
35
36
37
38
39
40
41
42
43
44
45
46
47
48
49
50
51
52
53
54
55
56
57
58
59
60
61
62
63
64
65

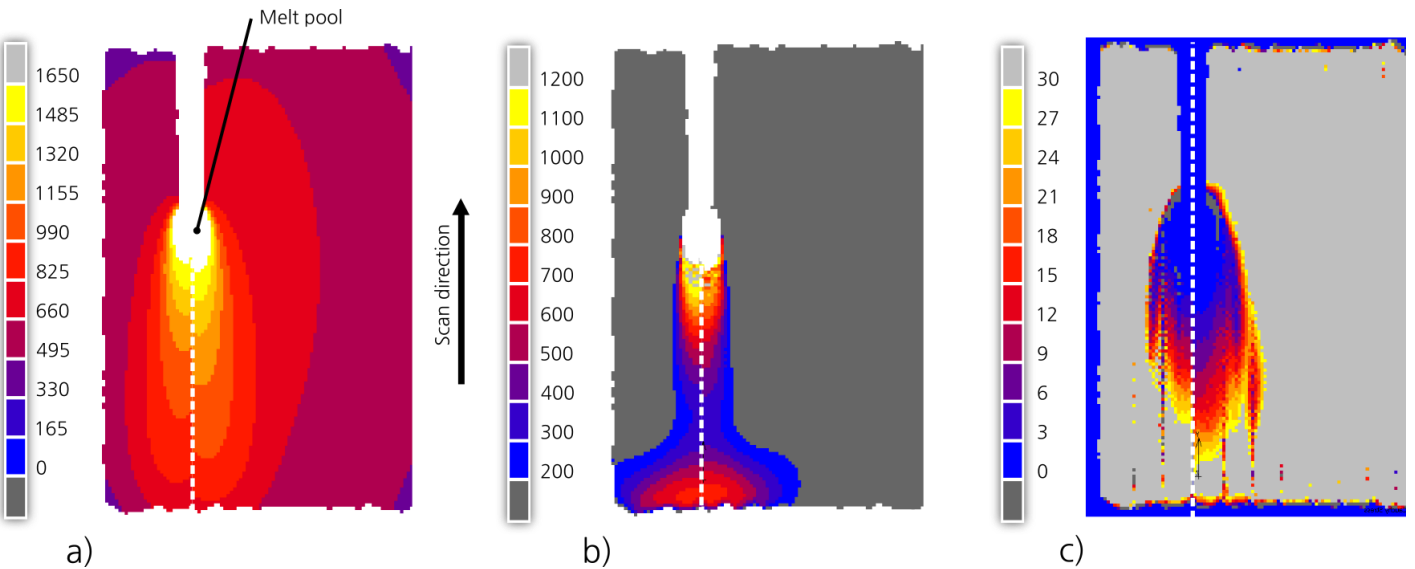


Figure 17 – Mirrored profile views of a) the temperature, b) the temperature gradient in the Y direction, and c) σ_{yy} taken at $t = 0.0320s$ (left half) and at $t = 0.156s$ (right half).

4.4 Comparison between Laser Scan Strategies

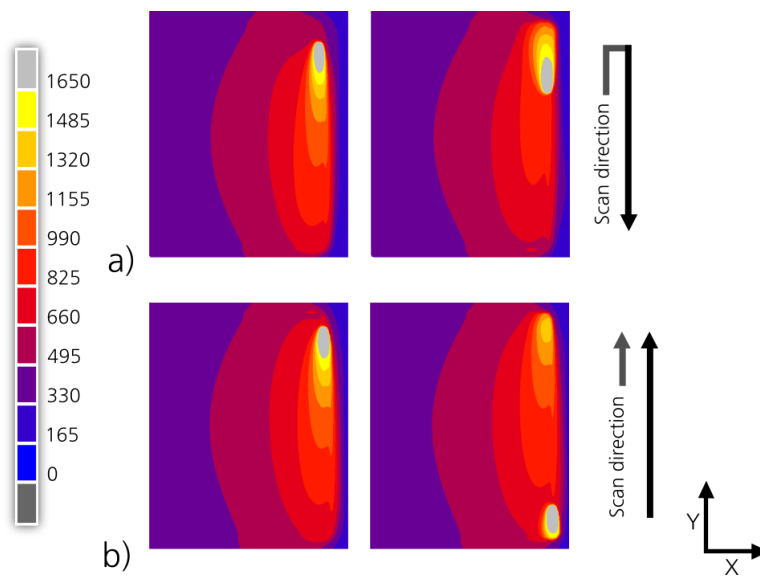
To enable comparison of the different scan areas sizes and scan strategies on the mechanical response, the mean values were calculated for the normal strain and stress components and the von Mises stress, which are listed in Table 7. The average values of these measurements were sampled from all consolidated elements on the final time step of the simulation.

Scan Area	Scan Strategy	Total Strain Component $\times 10^{-3}$			Stress Components [MPa]			Von Mises Stress [MPa]
		ϵ_{xx}	ϵ_{yy}	ϵ_{zz}	σ_{xx}	σ_{yy}	σ_{zz}	
1 mm x 1 mm	Alternate	-13.5	-9.0	-22.9	151.8	189.3	0.0	236.0
	Unidirectional	-13.8	-9.1	-22.5	145.1	183.6	0.0	221.0
2 mm x 2 mm	Alternate	-13.5	-6.2	-23.7	161.8	270.1	0.0	289.0
	Unidirectional	-13.5	-6.1	-23.4	166.8	273.5	0.0	289.3
3 mm x 3 mm	Alternate	-13.9	-4.5	-23.6	140.2	302.0	0.0	307.0
	Unidirectional	-13.8	-4.4	-23.5	143.9	305.2	0.0	307.0

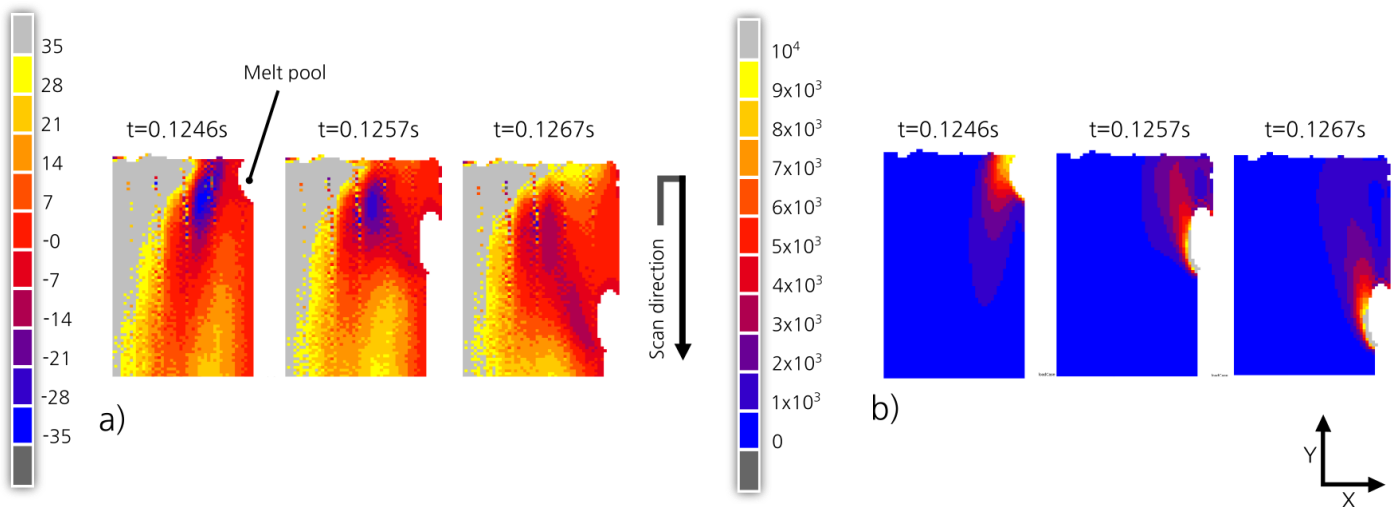
Table 7 - Average values for von Mises stress and normal strain and stress components calculated from solid elements located in the first layer for multiple simulation cases

The greatest strain component was ϵ_{zz} followed by ϵ_{xx} and ϵ_{yy} . The von Mises stress increases with the scan area size. Throughout each test case, the largest magnitude of stress exists in the σ_{yy} component, followed by σ_{xx} with a small value for the σ_{zz} component. Measuring the average for stress and strain, reveals no substantial difference between the two scan strategies, but, there is clearly a difference in the distribution of stress components, as shown in Figure 15 and Figure 16.

1 A comparison of the temperature at the start and the end of scan vectors between scan strategies is
 2 shown in Figure 18, to better understand the difference in the distribution of stress components
 3 during the process. When the alternating scan strategy was used, the next scan vector began in a
 4 higher temperature region compared to the unidirectional scan due to the prior scan vector finishing
 5 nearby. The elevated temperature in the alternate scan reduces the magnitude of the temperature
 6 gradient for the alternating scan, as shown in Figure 19(b), which is less at the start of the scan
 7 vector compared to the unidirectional scan shown in Figure 20(b). After the duration of 2 ms,
 8 the distributions of the temperature gradients become independent of their position along the scan
 9 vector for both scan strategies. The transverse stress at the start of the scan vectors differed
 10 between strategies. At the beginning of the scan vector, a larger region is subjected to a compressive
 11 transverse stress when using the alternating strategy, as shown in Figure 19(a), compared to the
 12 unidirectional strategy shown in Figure 20(a).



16
17
18
19
20
21
22
23
24
25
26
27
28
29
30
31
32
33
34
35
36
37 **Figure 18 - Profile view of temperature distribution at the approach and exit of the laser scan vector when using a)**
 38 **alternating scan strategy and b) unidirectional scan strategy.**



39
40
41
42
43
44
45
46
47
48
49
50
51
52
53
54
55
56
57
58
59 **Figure 19 - Profile views of a) σ_{xx} stress and b) temperature gradient for solid elements at the beginning of the scan**
 60 **vector using the alternating strategy**

61
62
63
64
65

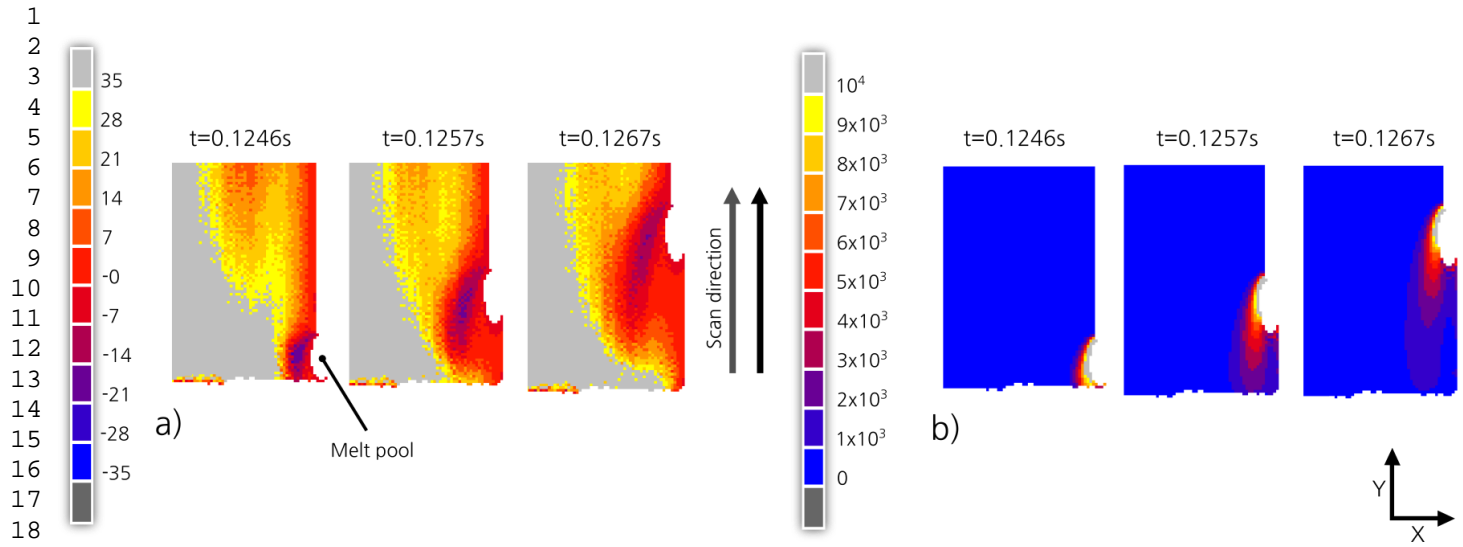


Figure 20 – Profile views of a) σ_{xx} stress and b) temperature gradient for solid elements at the beginning of the scan vector using the unidirectional strategy

The previously described temperature effect also caused a difference in the distribution of plastic strain between scan strategies. When using the unidirectional scan strategy, a uniform distribution of plastic strain is present throughout the hatch region, as shown in Figure 21(b), whereas the alternating scan strategy features decreased levels of plastic strain towards the end of the scan vectors, as shown in Figure 21(a).

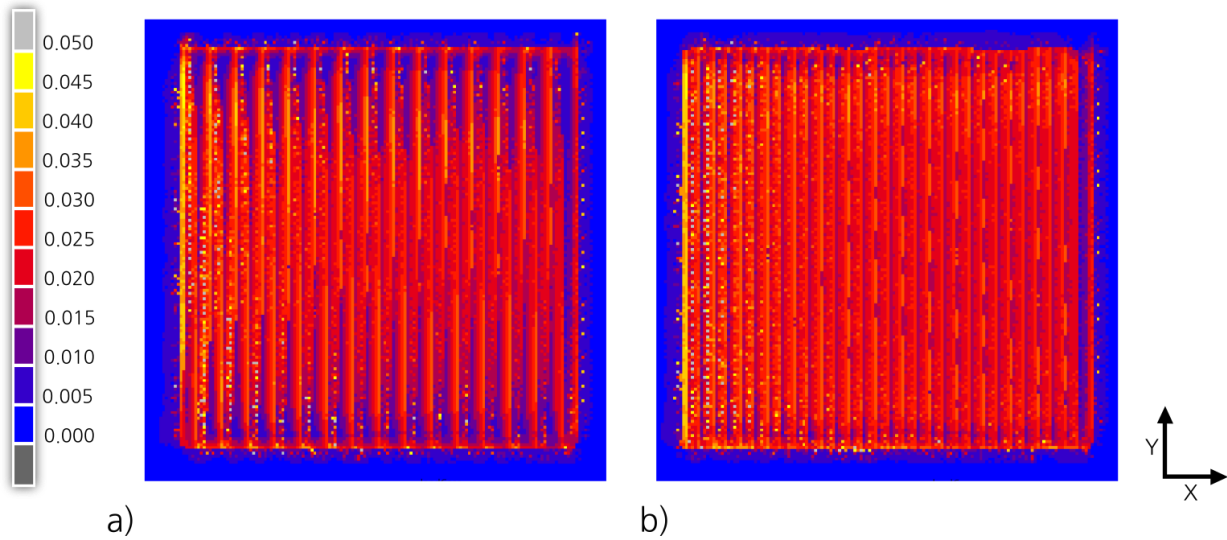


Figure 21 - Profile view of total equivalent plastic strain fields for a) alternating strategy and b) unidirectional strategy

5 Discussion

The single layer experiment showed that the melted track width varies with the experiment by 14%. However, potential error does exist in the experiment, such as accurately levelling the base plate, exact lens focal position, and inconsistency in the thickness of the powder layer created manually.

1 Nevertheless, the peak temperature is in good agreement with another work that used a similar
2 smaller spot size of 50 μm [37]. Currently, this work excludes the effect of vaporization although it is
3 acknowledged that accounting for this effect will influence the melt pool depth and geometry, and
4 limit the maximum surface temperature. This is not expected to cause a significant change in the
5 thermal and stress values reported by the simulation because the effect will be isolated to the
6 temperature singularity inside the melt pool, as shown in Figure 6.
7

8
9 The temperature history shown in Section 4.2 reveals the importance of the sizing effect in the
10 physical problem. It was found the temperature distribution achieved and length of time sustained is
11 dependent on the size of scan area, as shown in Figure 8 and Figure 11. The smallest scan area
12 sustains a high temperature for a short period but due to its size cools rapidly after scanning has
13 completed, whereas the largest region holds a lower temperature for longer with a lower cooling
14 rate. This is caused by the accumulation of thermal energy into the consolidated regions and
15 substrate over the duration of the scan.
16
17

18
19 A large proportion of material in the 1 mm x 1 mm test cases, as shown in Figure 11, is held above
20 the superplastic temperature. In Table 7, this test case has the greatest longitudinal strain (ϵ_{YY}), and
21 has the smallest transverse stress which indicates that plastic deformation has occurred. In super
22 plastic forming of Ti-6Al-4V, parts can be manufactured without suffering from residual stress or
23 spring back, at low shear rates [41] and likewise shows that the formation of residuals stresses can
24 be controlled by temperature. Depending on the substrate (powder or solid), varying the scan area
25 size will enable control over the sustained temperature achieved in a scanned region. Potentially,
26 this will enable control over the build-up residual stress and generation of the microstructure by
27 elevating the temperature and reducing the rate of cooling [42].
28
29
30
31

32 Oscillations in the temperature exist, as shown between Figure 8 and Figure 11, and have different
33 frequencies for the laser scan strategies due to the interval of time between adjacent scanning. The
34 period of the oscillations is, therefore, affected directly by the scan vector length. The unidirectional
35 strategy has a more stable minimum temperature, due to smaller time period between adjacent
36 scans, as shown in Figure 9 and Figure 11, but this also affected by the lack of thermal mass available
37 early in the scanning history. Also, it is evident in Figure 9 that the heating effect from the laser in
38 previously consolidated areas diminishes between three to four adjacent scan tracks, and this is also
39 visible in Figure 12. Potentially, a performance improvement for simulating SLM could be gained by
40 modelling regions far from the melt-pool using a steady-state analysis, but retaining the transient
41 behaviour in region near the melt-pool.
42
43
44
45
46

47 The analysis of stress in Section 4.3 showed the main contributor of stress is created parallel to the
48 scan vector. Observing the behaviour in a single scan track, the longitudinal stress was considerably
49 higher than the transverse stress, due the higher temperature gradient component parallel to the
50 scan vector, as shown in Figure 13(c). Table 7 shows that increasing the scan area size effectively
51 increases the overall stress in the region. This is caused by the dominating longitudinal stress which
52 increases with scan vector length as reported by literature [43]. Therefore when designing laser scan
53 strategies, it is important to minimise the scan vector lengths for all orientations.
54
55
56

57 For all test cases, a non-uniform anisotropic stress distribution was generated, as illustrated in Figure
58 15 and Figure 16. The calculated averages for the normal stress components match observations in
59 experimental studies using experimental X-ray diffraction measurements conducted by Simonelli et
60
61
62
63
64
65

1 al. [44] and numerically by Roberts [19]. Overall, the laser scan strategy chosen for a component
2 should factor in the anisotropic build-up of stress created during this process. A further study is
3 required to determine the viability of orientating the scan vectors in an optimal way to equalise the
4 overall stress field whilst considering other processing constraints such as porosity.
5

6 Longitudinal stress tended to decrease in the X direction and was caused by a combination of a
7 higher elevated temperature, and a lower temperature gradient, as shown in Figure 17. This
8 corresponds with the temperature history, as shown in Figure 10 with the region of higher
9 temperature (>825°C) increasing in area towards a plateau throughout the scanning history.
10

11
12 After successive scanning of tracks, as shown in Figure 14, the mechanism for the generation of
13 transverse stress was found to be caused by the temperature gradient mechanism shown in Figure
14 14(b). The thermal expansion of solid material surrounding the melt pool area creates a region of
15 compressive transverse stress (Figure 14(c)). Additionally, regions of plastic strain were created by
16 re-melting between adjacent scan tracks occurring at high temperature (Figure 14(d)). The
17 distributions of the total strain components correspond to the large values in the X and Z direction
18 for the total strains, as shown in Table 7, which includes contributions from the plastic strains. This
19 indicates that in a full sized part distortion will occur normal to the XY plane, where the total strain
20 component in the Z direction is greatest, which results in the 'curling' effect typically observed in
21 failed builds. These findings raise concerns about mechanical testing on as-built specimens produced
22 in SLM because they will contain geometrically dependent residual stress and plastic deformation,
23 which will affect the bulk material strength and ductility in the final component.
24
25

26
27 The average stresses calculated in Table 7 indicate that scanning small regions with the same laser
28 parameters for these two scan strategies do not strongly affect the magnitude of residual stress. This
29 was suspected to be caused by the small scale of the analysis. Nevertheless, a difference was shown
30 between the two scan strategies for the distribution of planar normal stresses, and the plastic strain
31 towards the end of the scan vectors, as shown in Figure 16 and Figure 21. The 'rippled' stress
32 distribution present in the alternating strategy is attributed to the reverse of the scan vector
33 direction. Both effects are caused by the high temperature and smaller temperature gradients found
34 in this region, as shown in Figure 18 , Figure 19, when using the alternating scan strategy. Inevitably,
35 increasing the substrate temperature prior to scanning will reduce the magnitude of residual stress
36 and plastic deformation in a part, as reported by other researchers [9,12]. This, however, is currently
37 not practical to perform with current commercial SLM technologies.
38
39
40
41
42
43
44
45

46 **6 Conclusions**

47
48 A coupled thermo-mechanical simulation has been established capable of predicting residual stress
49 for two different scan strategies for single layer cross-sections of 1-3 mm. This work demonstrates
50 that even at a macro scale, complex transient behaviour is inherent during the process of selective
51 laser melting. It has identified the interaction between temperature history and the mechanical
52 response and the effect of laser scan strategy on the stress distribution. Specific conclusions were
53 drawn from the research:
54
55
56
57

- 58 • The temperature oscillates with a frequency dependent on the scan vector length.
59
60
61
62
63
64
65

- The larger scanned regions had a lower average temperature but were sustained for a longer duration due to the accumulation of heat.
- Longitudinal stress (parallel to the scan vector) increases with scan vector length and is the main contribution to stress due to presence of the larger thermal gradient parallel to the scan vector.
- The process generates a non-uniform anisotropic stress field, which have regions of lower transverse and longitudinal stresses situated towards the end of the scan vectors.
- No substantial difference in the magnitude of stress was observed between the two scan strategies. However, the distribution of stress and plastic strain did vary between laser scan strategies and was shown to be caused by the thermal history.
- Reduced levels of stress and plastic strain are exhibited at the end of scan vectors when using the alternate scan strategy due to the reduced temperature gradients at the end of each vector.

Based on these findings, the design of laser scan strategies should avoid long scan vector lengths and orientate the direction of scan vectors uniformly to produce an isotropic stress field in the component. The size of the hatch regions should be varied appropriately, to sustain the highest elevated temperature without causing instability in the process. By combing this knowledge, optimising the laser scan strategy could further mitigate the effects of the residual stress and reduce support structure requirements without requiring changes to the SLM machine or design of the part manufactured.

7 References

- [1] Baumer M, Tuck C, Wildman R, Ashcroft I, Hague R. Shape Complexity and Process Energy Consumption in Electron Beam Melting. *Journal of Industrial Ecology* 2016;20:11.
- [2] Hopkinson N, Hague R, Dickens P. *Rapid manufacturing: an industrial revolution for the digital age*. John Wiley & Sons; 2006.
- [3] Brackett D, Ashcroft I, Hague R. Topology optimization for additive manufacturing. *Solid Freeform Fabrication Symposium*, 2011, p. 348–62.
- [4] Aremu A, Ashcroft I, Wildman R, Hague R, Tuck C, Brackett D. The Effects of Bidirectional Evolutionary Structural Optimization Parameters on an Industrial Designed Component for Additive Manufacture. *Proceedings of the Institution of Mechanical Engineers, Part B: Journal of Engineering Manufacture* 2013;227:794–807. doi:10.1177/0954405412463857.
- [5] Maskery I, Aremu AO, Simonelli M, Tuck C, Wildman RD, Ashcroft IA, et al. Mechanical Properties of Ti-6Al-4V Selectively Laser Melted Parts with Body-Centred-Cubic Lattices of Varying cell size. *Experimental Mechanics* 2015:1–12. doi:10.1007/s11340-015-0021-5.
- [6] ASTM. ASTM F2924-14, Standard Specification for Additive Manufacturing Titanium-6 Aluminum-4 Vanadium with Powder Bed Fusion. *ASTM Standards* 2014;10.04. doi:10.1520/F2924.
- [7] Edwards P, Ramulu M. Fatigue Performance Evaluation of Selective Laser Melted Ti-6Al-4V. *Materials Science and Engineering: A* 2014;598:327–37. doi:10.1016/j.msea.2014.01.041.
- [8] Kruth JP, Levy G, Klocke F, Childs THC. Consolidation phenomena in laser and powder-bed based layered manufacturing. *CIRP Annals - Manufacturing Technology* 2007;56:730–59.

doi:<http://dx.doi.org/10.1016/j.cirp.2007.10.004>.

- 1
2
3
4
5
6
7
8
9
10
11
12
13
14
15
16
17
18
19
20
21
22
23
24
25
26
27
28
29
30
31
32
33
34
35
36
37
38
39
40
41
42
43
44
45
46
47
48
49
50
51
52
53
54
55
56
57
58
59
60
61
62
63
64
65
- [9] Mumtaz K, Vora P, Hopkinson N. A METHOD TO ELIMINATE ANCHORS/SUPPORTS FROM DIRECTLY LASER MELTED METAL POWDER BED PROCESSES. *SFF*, 2011, p. 55–64.
 - [10] Simonelli M, Tse YY, Tuck C. On the texture formation of selective laser melted Ti-6Al-4V. *Metallurgical and Materials Transactions A: Physical Metallurgy and Materials Science* 2014;45:2863–72. doi:10.1007/s11661-014-2218-0.
 - [11] Aboulkhair NT, Everitt NM, Ashcroft I, Tuck C. Reducing porosity in AlSi10Mg parts processed by selective laser melting. *Additive Manufacturing* 2014;1-4:77–86. doi:10.1016/j.addma.2014.08.001.
 - [12] Mercelis P, Kruth J-P. Residual stresses in selective laser sintering and selective laser melting. *Rapid Prototyping Journal* 2006;12:254–65. doi:10.1108/13552540610707013.
 - [13] Hauser C, Chillds T, Dalgarno KW. Selective Laser Sintering of Stainless Steel 314S HC processed using room temperature powder beds. *Proceedings of the SFF Symposium* 1999:273–80.
 - [14] Pohl H, Simchi A, Issa M, Dias H. Thermal stresses in direct metal laser sintering. *Proceedings of the Solid Freeform ...* 2001:366–72.
 - [15] Vrancken B, Wauthle R, Kruth J, Humbeeck J Van. Study on the influence of material properties on residual stress in selective laser melting. *Lirias.kuleuven.be* 2013.
 - [16] Dai K, Shaw L. Thermal and mechanical finite element modeling of laser forming from metal and ceramic powders. *Acta Materialia* 2004;52:69–80. doi:10.1016/j.actamat.2003.08.028.
 - [17] Riedlbauer D, Steinmann P, Mergheim J. Thermomechanical finite element simulations of selective electron beam melting processes: performance considerations. *Computational Mechanics* 2014;54:109–22. doi:10.1007/s00466-014-1026-0.
 - [18] Hodge NE, Ferencz RM, Solberg JM. Implementation of a thermomechanical model for the simulation of selective laser melting. *Computational Mechanics* 2014;54:33–51. doi:10.1007/s00466-014-1024-2.
 - [19] Roberts IA. Investigation of Residual Stresses in the Laser Melting of Metal Powders in Additive Layer. University of Wolverhampton, 2012.
 - [20] Zaeh MF, Branner G. Investigations on residual stresses and deformations in selective laser melting. *Production Engineering* 2009;4:35–45. doi:10.1007/s11740-009-0192-y.
 - [21] Neugebauer F, Keller N, Xu H, Kober C, Ploshikhin V. Simulation of Selective Laser Melting Using Process Specific Layer Based Meshing. *Proceedings of the Fraunhofer Direct Digital Manufacturing Conference, Bremen: 2014*.
 - [22] Keller N, Ploshikhin V. New Method for Fast Predictions of Residual Stress and Distortion of AM Parts. *Solid Freeform Fabrication Symposium, Austin, Texas: 2014*, p. 1229–37.
 - [23] Jamshidinia M, Kong F, Kovacevic R. The Coupled CFD-FEM Model of Electron Beam Melting (EBM). *ASME District F - Early Career Technical Conference Proceedings, Birmingham: 2013*.
 - [24] Marimuthu S, Eghlio RM, Pinkerton AJ, Li L. Coupled Computational Fluid Dynamic and Finite Element Multiphase Modeling of Laser Weld Bead Geometry Formation and Joint Strengths. *Journal of Manufacturing Science and Engineering* 2013;135:11004.
 - [25] Gürtler F-J, Karg M, Leitz K-H, Schmidt M. Simulation of laser beam melting of steel powders using the three-dimensional volume of fluid method. *Physics Procedia* 2013;41:881–6.

- 1 [26] Khairallah S, Anderson A. Mesoscopic simulation model of selective laser melting of stainless
2 steel powder. *Journal of Materials Processing Technology* 2014;214:2627–36.
3 doi:10.1016/j.jmatprotec.2014.06.001.
- 4 [27] Realizer SLM 50. Realizer GmbH. Borchten, Germany: 2015
- 5 [28] MSC Marc 2014.2. MSC Software Corporation. Newport Beach, California, USA: 2015
- 6 [29] Liu B. Further Process Understanding and Prediction on Selective Laser Melting of Stainless
7 Steel 316L. University of Loughborough, 2013.
- 8 [30] Wood RA, Favor RJ, (U.S.) AFML. Titanium alloys handbook. Columbus, Ohio: Metals and
9 Ceramics Information Center; 1972.
- 10 [31] Boivineau M, Cagran C, Doytier D, Eyraud V, Nadal M-H, Wilthan B, et al. Thermophysical
11 Properties of Solid and Liquid Ti-6Al-4V (TA6V) Alloy. *International Journal of Thermophysics*
12 2006;27:507–29. doi:10.1007/s10765-005-0001-6.
- 13 [32] Alderson NA. Thermal Modeling and Simulation of Electron Beam Melting for Rapid
14 Prototyping on Ti6Al4V Alloys. North Carolina State University, 2012.
- 15 [33] Goldak J, Chakravarti A, Bibby M. A new finite element model for welding heat sources.
16 *Metallurgical Transactions B* 1984;15:299–305. doi:10.1007/BF02667333.
- 17 [34] Tolochko NK, Khlopkov Y V., Mozharov SE, Ignatiev MB, Laoui T, Titov VI. Absorptance of
18 powder materials suitable for laser sintering. *Rapid Prototyping Journal* 2000;6:155–61.
19 doi:10.1108/13552540010337029.
- 20 [35] Fischer P, Romano V, Weber HP, Karapatis NP, Boillat E, Glardon R. Sintering of commercially
21 pure titanium powder with a Nd:YAG laser source. *Acta Materialia* 2003;51:1651–62.
22 doi:10.1016/S1359-6454(02)00567-0.
- 23 [36] Simonelli M, Tuck C, Aboulkhair NT, Maskery I, Ashcroft I, Wildman RD, et al. A Study on the
24 Laser Spatter and the Oxidation Reactions During Selective Laser Melting of 316L Stainless
25 Steel, Al-Si10-Mg, and Ti-6Al-4V. *Metallurgical and Materials Transactions A* 2015.
26 doi:10.1007/s11661-015-2882-8.
- 27 [37] Fu CH, Guo YB. Three-Dimensional Temperature Gradient Mechanism in Selective Laser
28 Melting of Ti-6Al-4V. *Journal of Manufacturing Science and Engineering* 2014;136:061004.
29 doi:10.1115/1.4028539.
- 30 [38] Chakrabarty J. Applied plasticity. 2nd Ed. Boston: Springer; 2010.
- 31 [39] Deng D, Murakawa H, Liang W. Numerical and experimental investigations on welding
32 residual stress in multi-pass butt-welded austenitic stainless steel pipe. *Computational*
33 *Materials Science* 2008;42:234–44. doi:10.1016/j.commatsci.2007.07.009.
- 34 [40] Rangaswamy P, Choo H, Prime MB, Bourke MAM, Larsen JM. High Temperature Stress
35 Assessment in SCS-6/Ti-6Al-4V Composite using Neutron Diffraction and Finite Element
36 Modeling. *International Conference on Processing & Manufacturing of Advanced Material*,
37 Los Alamos: 2000.
- 38 [41] Liu J, Tan M-J, Aue-u-lan Y, Guo M, Castagne S, Chua B-W. Superplastic-like forming of Ti-6Al-
39 4V alloy. *The International Journal of Advanced Manufacturing Technology* 2013;69:1097–
40 104. doi:10.1007/s00170-013-5101-z.
- 41 [42] Buchbinder D, Meiners W, Pirch N, Wissenbach K, Schrage J. Investigation on reducing
42 distortion by preheating during manufacture of aluminum components using selective laser
43 melting. *Journal of Laser Applications* 2014;26:012004. doi:10.2351/1.4828755.
- 44
45
46
47
48
49
50
51
52
53
54
55
56
57
58
59
60
61
62
63
64
65

[43] Gibson I, Rosen DW, Stucker B. Additive Manufacturing Technologies. vol. 54. Boston, MA: Springer US; 2010. doi:10.1007/978-1-4419-1120-9.

[44] Simonelli M. Microstructure Evolution and Mechanical Properties of Selective Laser Melted Ti-6Al-4V. University of Loughborough, 2014.

1
2
3
4
5
6
7
8
9
10
11
12
13
14
15
16
17
18
19
20
21
22
23
24
25
26
27
28
29
30
31
32
33
34
35
36
37
38
39
40
41
42
43
44
45
46
47
48
49
50
51
52
53
54
55
56
57
58
59
60
61
62
63
64
65